Article

Adsorption and Photocatalytic Properties of Tris(4-aminophenyl)amine-based Polyimide/Graphitic Carbon Nitride Composites for Organic Dye Removal

Umama Binte Irshad, Zareen Akhtar, Götz Bucher, Alexey Y. Ganin, Humaira Masood Siddiqi,* and Bernhard V. K. J. Schmidt*
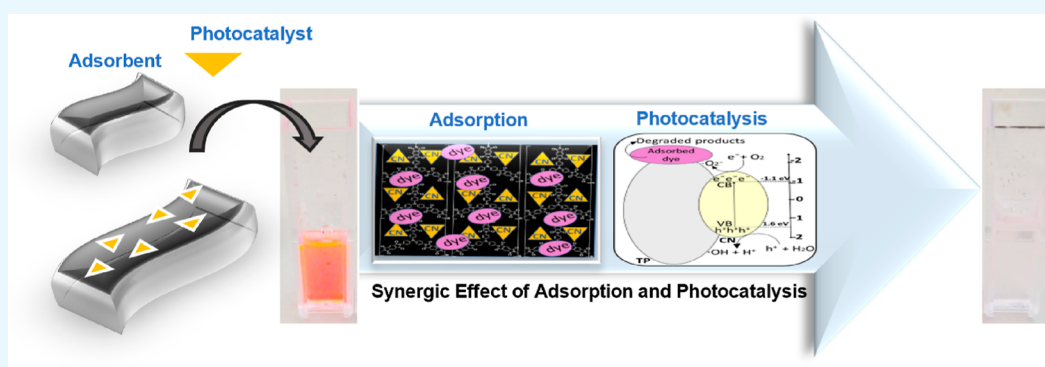
Cite This: https://doi.org/10.1021/acsapm.4c00019

Read Online

ACCESS | Metrics & More | Article Recommendations | Supporting Information

Synergic Effect of Adsorption and Photocatalysis

ABSTRACT: Adsorption and degradation of harmful organic molecules in aqueous wastewater streams is a considerable challenge, and materials featuring both properties are highly sought after. Tris(4-aminophenyl)amine-based polyimide (TP) is well-known for its significant adsorption properties, yet it features limited photocatalytic performance. To overcome this limitation, graphitic carbon nitride (CN) is combined with TP to form TPCN composites in order to improve the adsorption and photocatalytic properties for the degradation of organic molecules. Characterization of TPCN composites via UV−vis diffuse reflectance spectra (DRS) and photoluminescence (PL) showed improved charge separation, slow recombination of electron−hole pairs, and enhanced light absorption. Subsequent analysis of rhodamine B adsorption and photodegradation showed high activity of the composite material (99% degradation under visible light in 40 min), indicating the favorable interaction of both components. Therefore, TPCN composites might be an avenue for the application of organic industrial pollutant removal.

KEYWORDS: adsorption, photocatalysis, polymer composites, dye degradation, water remediation

INTRODUCTION

Water pollution is one of the significant daily threats the world population faces and requires immediate attention. In response to this issue, numerous countries and environmental protection agencies are implementing stringent effluent standards to mitigate the challenges arising from water pollution.[1] As a result, wastewater contaminated with hazardous materials, such as dyes and metal ions, from a wide range of industries, including electroplating, metal forming, microelectronics, paper, and textiles, must be treated before they are discharged. Dye contaminated wastewater poses a serious threat to both the ecosystem and humans. It is estimated that 100,000 different types of dyes have been sold worldwide, and that 700,000 tons of dyes are produced every year.[2,3] Several dyes are lethal to aquatic plants, as they hinder photosynthesis in these organisms. Wastewater contaminated by organic dyes features increased chroma, which prevents sunlight penetration in the environment. In addition, due to functional groups like

biphenyl, naphthalene, etc., dyes also comprise carcinogens and mutagens.[4] Thus, the existence of highly toxic and nondegradable azo and aromatic structures in dye compounds can cause ecological destruction and pose potential hazards to humans. For instance, methylene blue is capable of causing permanent harm to the eyes, a burning sensation if ingested, and may induce symptoms like nausea, vomiting, and profuse sweating.[5] Another example is rhodamine B (RhB), which is a water-soluble dye used in the textile industry that can trigger skin and eye irritation.[6] Consequently, there is an increasing

Scheme 1. Top Left: Composite Formation; Top Right: Degradation of RhB; Bottom: Adsorption and Photocatalysis by Tris(4-aminophenyl)amine-Based Polyimide (TP) and Graphitic Carbon Nitride (CN) Composites (A: electron acceptor; D: electron donor)
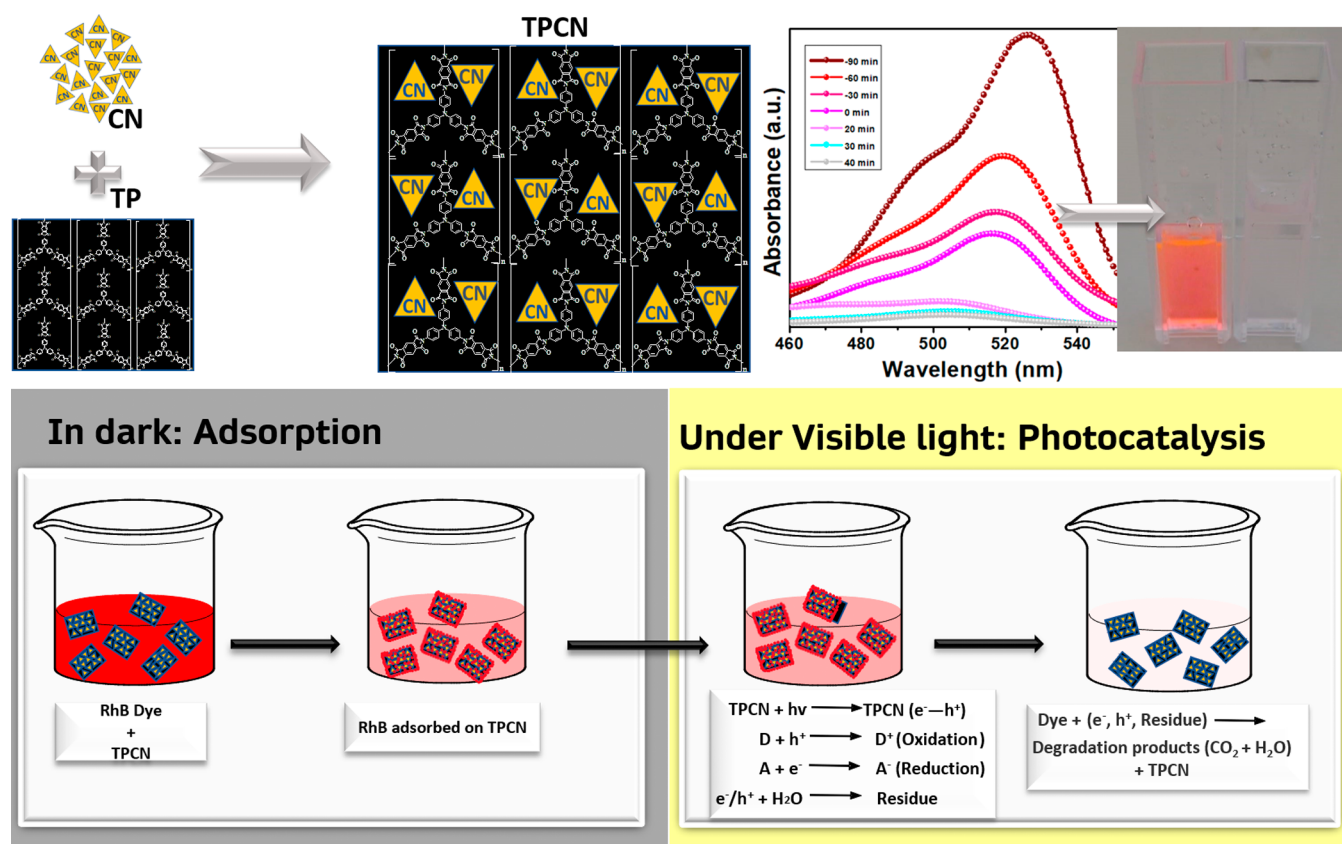
need to develop advanced wastewater treatment technologies that are environmentally friendly and capable of effectively treating harmful substances present in wastewater. Various technologies for the removal of dyes from water were developed, for example, adsorption, biological degradation, electrochemical degradation, photodegradation, and chemical oxidation.[7−11] Each type of treatment has its own benefits and drawbacks. In particular, adsorption is regarded as a reliable treatment owing to simple processing and low cost, but it is connected with the production of solid waste in significant amounts.[7]

In recent times, polymers have garnered significant attention as viable materials for water treatment due to their advantageous characteristics such as low toxicity, customizable functionalities, and cost-effectiveness.[12] Certain polymers exhibit a branch-like structure, falling into categories like dendronized, multiarmed star, and hyperbranched polymers. Among these groups, the branched structure of polymers (including their composites) has been of particular interest for their potential applications in wastewater treatment.[13]

Introduction of tris(4-aminophenyl)amine (TAPA) moieties into a polymer leads to a highly branched structure due to its propeller-shaped conformation and C3-symmetric structure.[14] The propeller-like shape disrupts polymer chain entanglement and increases the free volume of the polymer chain to improve adsorption capacity.[15] A profusion of functional groups and internal cavities makes polymers ideal for constructing templates to prepare nanoparticles with a higher adsorption capacity. For instance, hyperbranched polyimide, which has well-developed cavities, contains many nitrogen atoms. The

presence of such functional groups enhances the affinity of polyimides for pollutants.[16]

Photocatalysis is regarded as a green, efficient, eco-friendly, and promising wastewater treatment technique.[17,18] Numerous photocatalysts have been developed in the past, e.g., ZnO,[19] WO$_3$,[20] TiO$_2$,[21] SnO$_2$,[22] Fe$_2$O$_3$,[23] BiVO$_4$,[24] Ag$_3$PO$_4$,[25] and graphitic carbon nitride (CN).[26] CN consists of tri-s-triazines that are connected by tertiary aminess.[26] Additionally, CN is a typical polymeric semiconductor, possessing a layered, two-dimensional structure formed by the sp^2 hybridization of nitrogen and carbon, and forming π-conjugated graphitic planes.[27] In contrast to TiO$_2$, which is only active in the UV region, CN has a band gap of 2.7 eV, the conduction band (CB), and valence band (VB) positions are approximately −1.1 and +1.6 eV, respectively, versus the normal hydrogen electrode (NHE).[28] This enables it to be a visible-light-active photocatalyst for a range of reactions. Thus, compared with other photocatalysts, CN is more conveniently stimulated by visible light, leading to an increased activation efficiency for molecular oxygen producing active oxygen species such as •OH and •O$^{2−}$.[29] These active oxygen species are highly oxidizing, which benefits the photocatalytic conversion of organic functional groups and the degradation of organic molecules. In particular, CN is employed frequently as a visible-light photocatalyst due to its unique semiconductor band structure and excellent chemical stability,[30] which was pioneered in 2006 by Wang et al. Thus, CN has been extensively used for photocatalytic degradation, water splitting, photocatalytic reduction of CO$_2$, fuel cells, and environmental

Scheme 2. Synthesis Route of (a) Triamine TAPA and (b) Polyimide TP
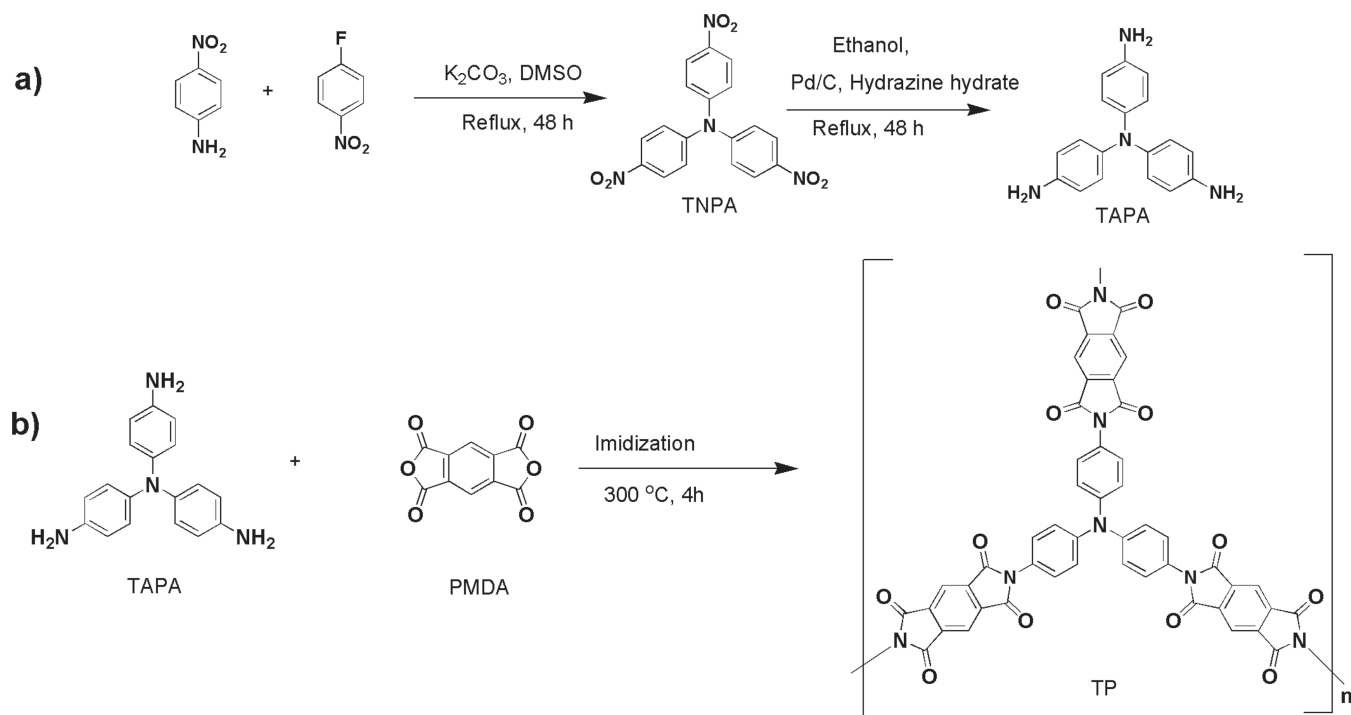
remediation.[31−33] With these highly relevant applications in mind, CN-based catalysts have been improved in various directions over the past few years. For example, variation in CN structures have been investigated like poly(heptazine imide)s or poly(triazine imide)s, but also structuring via nanosheet or nanosphere formation.[34,35] Nevertheless, the low surface area and fast recombination of photogenerated electron−hole pairs in pure CN restrict further improvement of its photocatalytic activity, leading to the requirement of further developments, e. g., functionalization, modification, or composite formation.[32,36]

As heterogeneous photocatalysis mainly depends on reactions at the interface, an optimum degradation capacity is obtained when pollutants are transferred to the surface of the catalyst directly. In other words, the excellent adsorption capacity of photocatalysts benefits the photodegradation process. Although, adsorption is one of the most efficient methods for removing pollutants, it cannot convert pollutants into harmless substances. Thus, adsorption can lead to secondary pollution, generation of waste adsorbent, and hence, limited utility. On the basis of the aforementioned factors, a synergistic strategy combining adsorption and photocatalysis is an avenue to improve pollutant removal.[4]

The main objective of this work was to synthesize a polymeric organic network composite system featuring TAPA-based polyimide (TP) and CN for use in the degradation of organic pollutants. TP and CN were synthesized by solid state polymerization, and the composite was formed via ultrasound treatment. TP, CN, and composites were characterized by powder X-ray diffraction (XRD), scanning electron microscopy (SEM), Fourier transform infrared (FTIR) spectroscopy, UV−vis diffuse reflectance spectroscopy (DRS), and photoluminescence (PL) spectroscopy to evaluate their crystallinity, morphology, chemical functionality, band gaps, and charge separation properties, respectively. Their dye removal efficiencies were assessed by determining adsorption and photocatalytic degradation using RhB in water as a representative organic pollutant (Scheme 1).

■ RESULTS AND DISCUSSION

Synthesis of TPCN Composites. Carbon nitride and TAPA-containing polyimide were synthesized to form photocatalytic composites. As shown in (Scheme 2a), the monomer for TP synthesis, TAPA, was synthesized through a two-step synthetic route. First, the nucleophilic substitution reaction of 4-nitroaniline with 4-fluoronitrobenzene in the presence of potassium carbonate gave the trinitro compound tris(4-nitrophenyl)amine (TNPA). The triamine monomer TAPA was obtained by reducing TNPA using hydrazine monohydrate catalyzed by Pd/C. The aromatic triamine monomer is pure enough for polymerization with the commercial aromatic dianhydride monomer pyromellitic dianhydride (PMDA) to prepare polyimides (Scheme 2b). The synthesis of TP was carried out at 300 °C, where the melted PMDA acts as a reactant and a reaction medium. Thus, the use of toxic high boiling-point solvents as well as the removal of solvent was avoided. During the preparation process, the polycondensation of TP is accompanied by dehydration, and the water molecules produced in the imidization reaction are evaporated rapidly at the reaction temperature, further promoting the condensation reaction between TAPA and PMDA. After the condensation of TAPA and PMDA, a blackish polyimide product was produced. Due to the densely cross-linked structure, the obtained TP exhibits excellent solvent-stability; i.e., it is insoluble in aqueous medium and other common organic solvents, including methanol, dimethylformamide, tetrahydrofuran, and in dimethyl sulfoxide.

Further, Fourier transform infrared (FTIR) spectroscopy studies were carried out to confirm the successful synthesis. For TAPA, the resultant product has characteristic peaks at 3405, 3330, 1615, and 1500 cm^{-1} which can be attributed to the N−H stretching vibration of primary amine, C=C
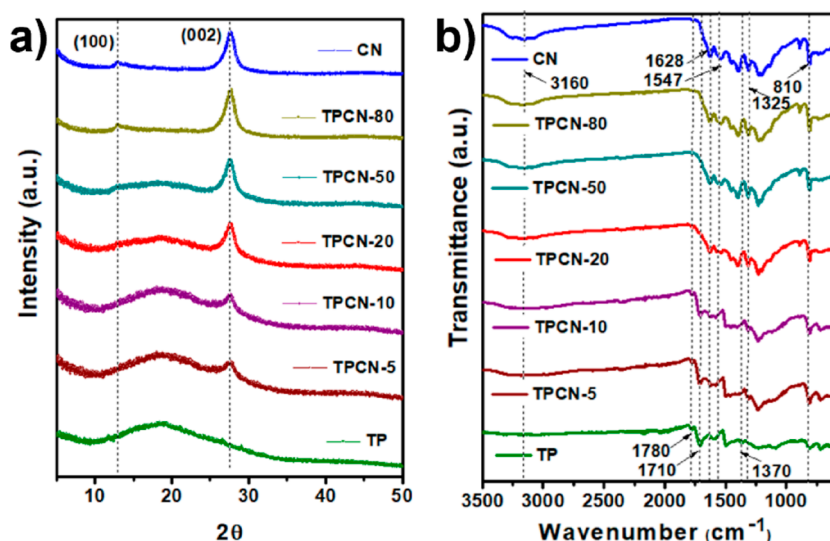
Figure 1. (a) XRD patterns of TP, CN, and TPCN composites within the range 2θ = 5−50°. (b) FTIR spectra of TP, CN, and TPCN composites.
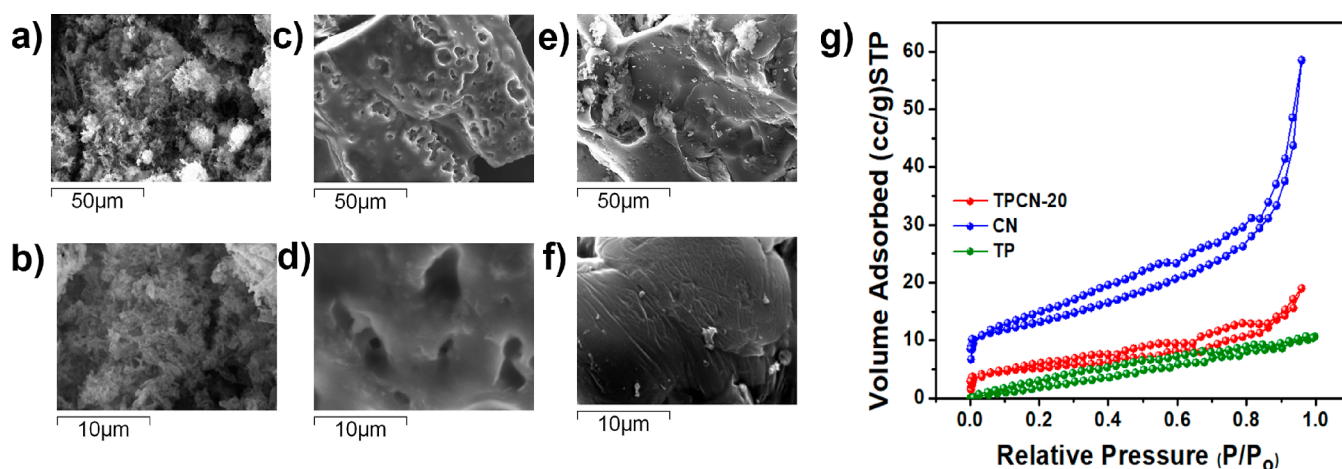

Figure 2. SEM images of (a,b) sponge-like CN particles, (c,d) smooth surfaced TP with cavities, and (e,f) TPCN-20 at different resolutions. (g) N_2 adsorption−desorption isotherms of CN, TP, and TPCN-20.

stretching vibration, and the C−C bending vibration of aromatic ring, respectively. The disappearance of the N−H peak and appearance of peaks of imide group confirms the synthesis of TP (Figure S1).[14] Further analysis via solid-state ^{13}C NMR confirmed the formation of TP (Figure S2).

CN was synthesized from the cyanuric acid-melamine complex via heat treatment in a tube furnace. For composite formation, CN and TP were combined through strong intermolecular forces such as hydrogen bonding and $\pi-\pi$-stacking interactions between the materials. The lone electron pairs of the free amino groups on the TAPA building block possess binding affinity for pollutants due to the Lewis acid base interactions, providing enhanced adsorption of TPCN composites for dyes. Polyimide/CN (TPCN-X) composites with varying weight ratios were formed using ultrasonication, where X reflects the amount of CN in wt %.

Crystallinity and Surface Morphology Analysis. Powder XRD measurements determined the crystallinity of the synthesized TP, CN, and TPCN composites (Figure 1a). As expected from literature,[37] the diffraction pattern of TP showed a completely amorphous nature of the polymer as indicated by the presence of a broad feature between 12 and 30°, which is due to the presence of bulky triphenylamine groups disrupting the chain packing and inhibiting the formation of ordered structure formation. For CN, two pronounced diffraction peaks at around 13.1 and 27.5° correspond to the (100) and (002) planes, respectively. These two peaks are attributed to the structure of the tri-*s*-triazine units with interplanar spacing and the conjugated aromatic system.[38] For TPCN composites, the crystallinity increased with an increment in CN loading as indicated by an increase in the intensity of the (002) peak and a decrease in the broad feature of TP (from TPCN-5 to TPCN-80) compared to the reflections from CN, which indicates an increasing presence of CN particles in the composites. To confirm the increase in crystallinity, full width at half-maximum (fwhm) was calculated from the fitting of the peak at ca. 27.5° with the Gaussian function. The decrease in fwhm values confirms improved crystallinity of the products as CN added to TP (Table S1).

FTIR spectra to confirm the synthesis of composites are given below (Figure 1b). For TP as expected from the literature,[39] the characteristic absorption bands of the imide group at 1780, 1710, and 1370 cm^{-1} are observed. The
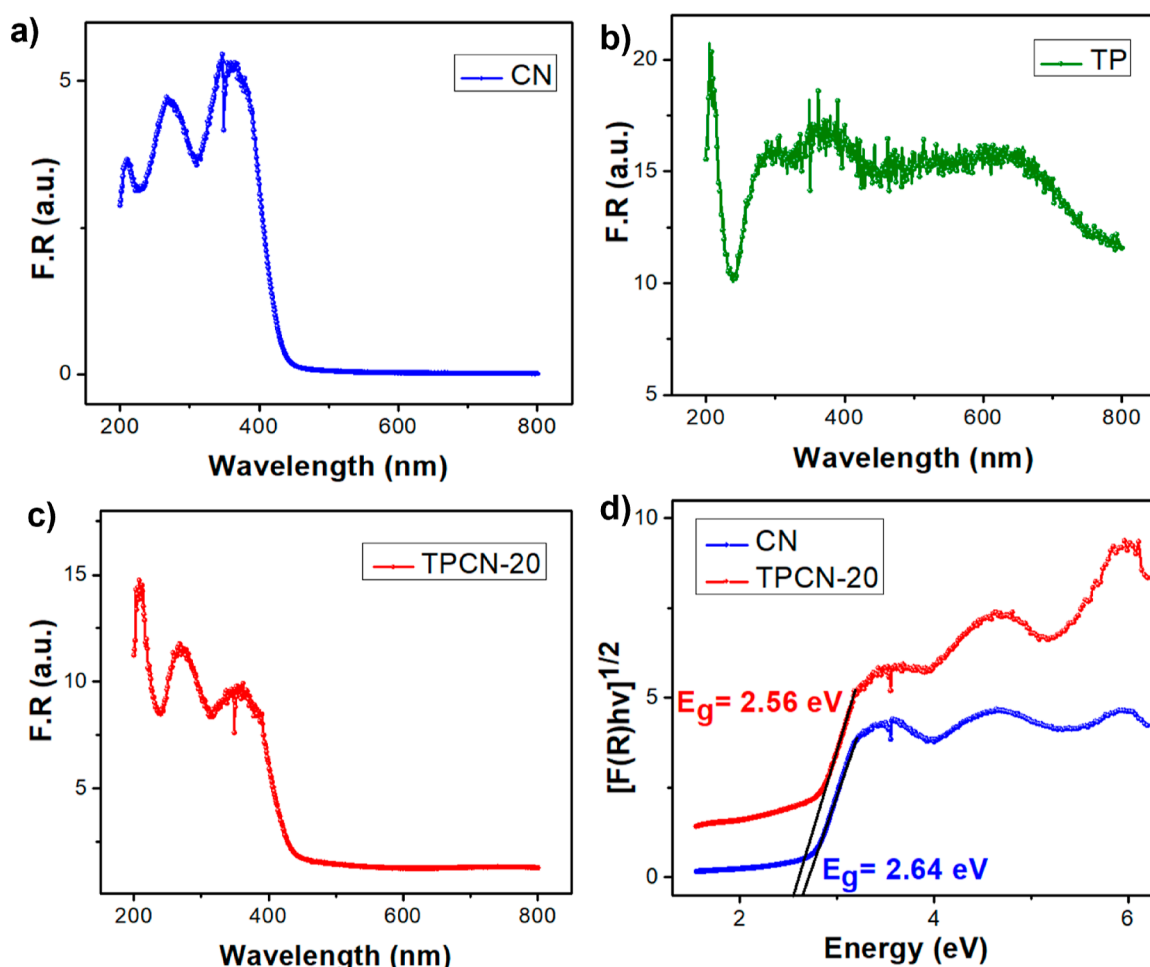
Figure 3. (a) UV−vis diffuse reflectance spectra of CN, (b) UV−vis diffuse reflectance spectra of TP, (c) UV−vis diffuse reflectance spectra of TPCN-20 (d), and band gap values assessed by a correlated curve of $(F(R)h\nu)^{1/2}$ set against photon energy plots of CN, and the composite TPCN-20.

spectrum of CN clearly shows several bands at the frequency, characteristics of vibrational modes related to the chemical bond between carbon and nitrogen,[40] as well as the broad band near 3160 cm^{-1} that is ascribed to the stretching vibration of N−H groups. While the strong bands in the range of 1200−1650 cm^{-1} with characteristic peaks at 1241, 1325, 1414, 1547, and 1628 cm^{-1} are attributed to the typical stretching vibration of C−N and C=N in the heterocyclic ring. The characteristic peak at 810 cm^{-1} is assigned to the breathing mode of the triazine units. For TPCN composites, the major peaks of both components, i.e., TP and CN, are observed. As the content of CN particles increased, the intensity of CN characteristic bands gradually became stronger and imide bands disappeared moving from TPCN-5 to TPCN-80.

The TPCN composites were further characterized regarding the surface morphology using scanning electron microscopy (SEM). For comparative morphological studies, the SEM micrographs at two different resolutions are shown in Figure 2a−f. It can be seen that CN has a sponge-like particle structure (Figure 2a,b). The morphology of TP (Figure 2c,d) appeared as a smooth surface with more or less homogeneous cavities. These cavities result most likely from the evaporation of condensation products during the imidization process at a high temperature.[41] When CN was introduced into the TP materials, some significant changes in the morphology of TP

are visible, although CN accounted for only a small amount of the material in TPCN-20 (Figure 2e,f). The images indicate CN particles are found to be well distributed over the polymer matrix. This leads to an increased number of active sites in the TPCN-20 composite that now has both the characteristics of TP (adsorbent) and CN (photocatalyst).

As adsorption capacity toward organic pollutants is connected to the surface area, we measured N$_2$ adsorption− desorption isotherms (Figure 2g). The Brunauer−Emmett− Teller (BET) approach was then used to calculate the surface area of pure TP, pure CN, as well as the TPCN-20 composite (Figure 2g). CN has the highest BET surface area (44.7 m^2 g^{-1}) that is close to the reported value in the literature,[42] whereas TP exhibits the lowest surface area (13.2 m^2 g^{-1}). The addition of CN to TP leads to an increase in the surface area for TPCN-20 to 17.4 m^2 g^{-1}, which can be attributed to the addition of more porous CN to the TP matrix.

UV−vis diffuse reflectance spectroscopy was used to measure the absorption characteristics of pristine CN, TP, and composite TPCN-20 (Figure 3). The absorption edge of pure CN was estimated to be around 450 nm (Figure 3a), while pure TP shows broad absorption in the visible region with high intensity (Figure 3b). TPCN-20 shows characteristic absorptions of TP and CN, whereas the absorption edge for TPCN-20 shows a slight blueshift due to the strong interaction

of TP and CN. The intensity of absorption for TPCN-20 is greater than CN which confirms the addition of TP to CN. The band gap energy of the composite and CN was evaluated using the following equation

$$\alpha h\nu = A(h\nu - E_g)^{1/2}$$

where A is constant, $h\nu$ is photon energy, and E_g is the band gap energy. E_g was observed from the extrapolation of Tauc plot when the curve $(\alpha h\nu)^{1/2}$ intersects the y-axis and an indirect band gap was assumed. The band gaps were estimated to be at 2.64 and 2.56 eV for CN and TPCN-20, respectively (Figure 3d). These band gap values are similar to the literature for CN and allow catalytic activity in the visible light region.[28] The band gap energies decreased in the composite on mixing of TP and CN, which might feature improved photocatalytic activity for the degradation of organic molecules under visible-light exposure.

A PL study at ambient temperature and excitation at a wavelength of 300 nm was used to investigate the separation efficiency of photo generated electron−hole pairs of CN, TP, and TPCN-20 (Figure 4a). A strong PL emission peak is
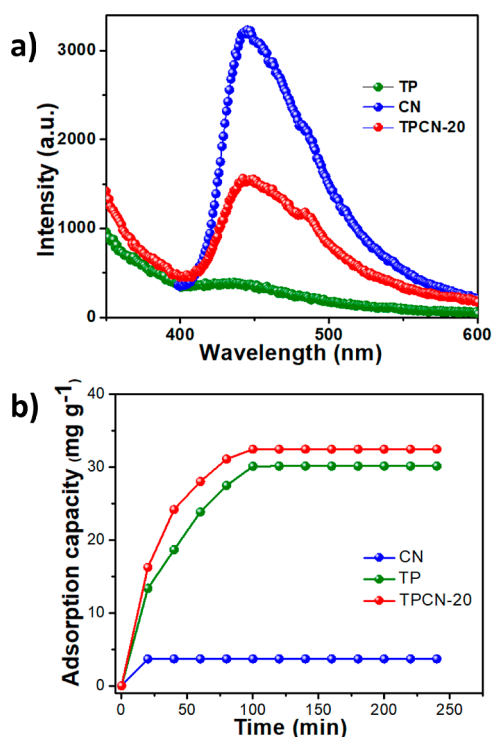

Figure 4. (a) PL spectra of TP, CN, and TPCN-20 at ambient temperature at an excitation wavelength of 300 nm. (b) Adsorption capacity (mg g^{-1}) of pure TP, CN, and TPCN-20 at ambient temperature in the dark (composite concentration: 0.5 mg mL^{-1} in 20 μM RhB solution).

observed for CN which can be attributed to the high recombination rate of photoinduced electrons and holes. Moreover, a very low PL emission was observed for TP because TP absorbs over the whole spectrum. The PL emission peak intensity for the TPCN-20 composite is significantly weaker than the PL intensity for CN implying that a heterogeneous structure is formed.

In order to gain a deeper insight into the photochemical behavior of TP, we performed DFT calculations. We optimized

the lowest triplet excited state of a model compound, TPI (Figure S3), using a DFT method (CAM-B3LYP/cc-pVDZ) (Tables S2 and S3). Solvation by a polar solvent (CH$_3$CN) was taken into account using a polarizable continuum model. According to the calculations, the sum of the Mulliken charges of the atoms of the central triphenylamine unit, in the lowest triplet state, is +1.46. For the ground-state of TPI, at the same level of theory, the calculation gives a sum of the Mulliken charges on the atoms of the triphenylamine unit of +0.67. Thus, the triplet state has an energy of 42.6 kcal mol^{-1}, which is a rather low energy. The DFT data were further corroborated by performing DLPNO−CCSD(T)/def2-TZVP-(CPCM,CH$_3$CN) single point energy calculations based on the geometries obtained by DFT. At this advanced level of theory, the sum of Mulliken charges on the central triphenylamine unit of TPI was obtained as 0.36 for the S$_0$ state, and 1.15 for the T$_1$ state. The T$_1$ energy was calculated as 48.0 kcal mol^{-1}. Hence, the calculations, both DFT and coupled-cluster, give support of the assumption from the literature[43] that TP-like structures undergo charge transfer.

Adsorption Properties of TPCN Composites. The adsorption performance was investigated by adsorption kinetics and adsorption isotherms. Among all composite samples, TPCN-20 was selected as a representative sample and its adsorption performance was evaluated against pure TP and CN samples.

Figure 4b shows the effect of contact time and adsorption capacities (q_t) on the surface of pure CN, pure TP, and TPCN-20 composite for the adsorption of RhB. In the beginning, TP and TPCN-20 show a more rapid adsorption compared to pure CN, indicating the excellent adsorption properties of TP. Afterward, the adsorption rate slows down until it reaches an equilibrium adsorption−desorption stage after 100 min when all the active sites are covered. This can be explained as in the initial adsorption stage, dye molecules will find their best orientation for strong binding on the extensively available catalyst surface. Eventually, the approach of dye molecules from the bulk solution will become more restricted due to the steric hindrance of adsorbed dye molecules already occupying surface sites. Hence, the rate of adsorption gradually decreases[44] as the maximum adsorption capacity of the catalyst is reached. Pure CN material does not show strong adsorption of RhB even though it has a higher BET surface area, which indicates that the adsorption of RhB on TPCN composites is only marginally related to the surface area but rather relies on surface chemistry. It is observed that TPCN-20 achieves the highest adsorption efficiency (75%) as compared to TP (73%) and CN (9.1%) with adsorption capacities of 32.7, 30.1, and 3.7 mg g^{-1}, respectively.

In order to study the relation between quantity of adsorbent and equilibrium concentration, adsorption isotherms were investigated.[45] The Freundlich and Langmuir models were studied here, showing the most accurate results for the Freundlich model (details about the models and results for the Langmuir model are discussed in the Supporting Information, Figure S4 and Table S4). The Freundlich isotherm describes nonideal adsorption on heterogeneous surfaces, where the adsorption capability is mainly related to the adsorbent concentration at equilibrium. Its linear form is given below:
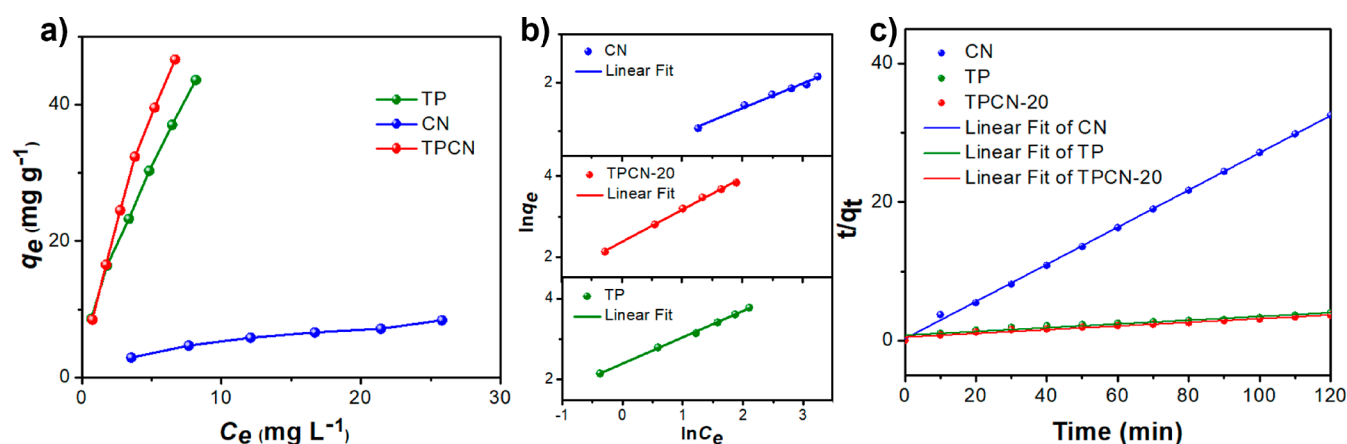
$$\ln q_e = \ln K_f + \frac{1}{n}\ln C_e$$

Figure 5. (a) Adsorption isotherms at equilibrium, (b) Freundlich isotherms, and (c) pseudo-second-order kinetics. Linear plots for TP (green), CN (blue), and TPCN-20 (red) with a concentration of 0.5 mg mL^{-1} in RhB solution at ambient temperature.
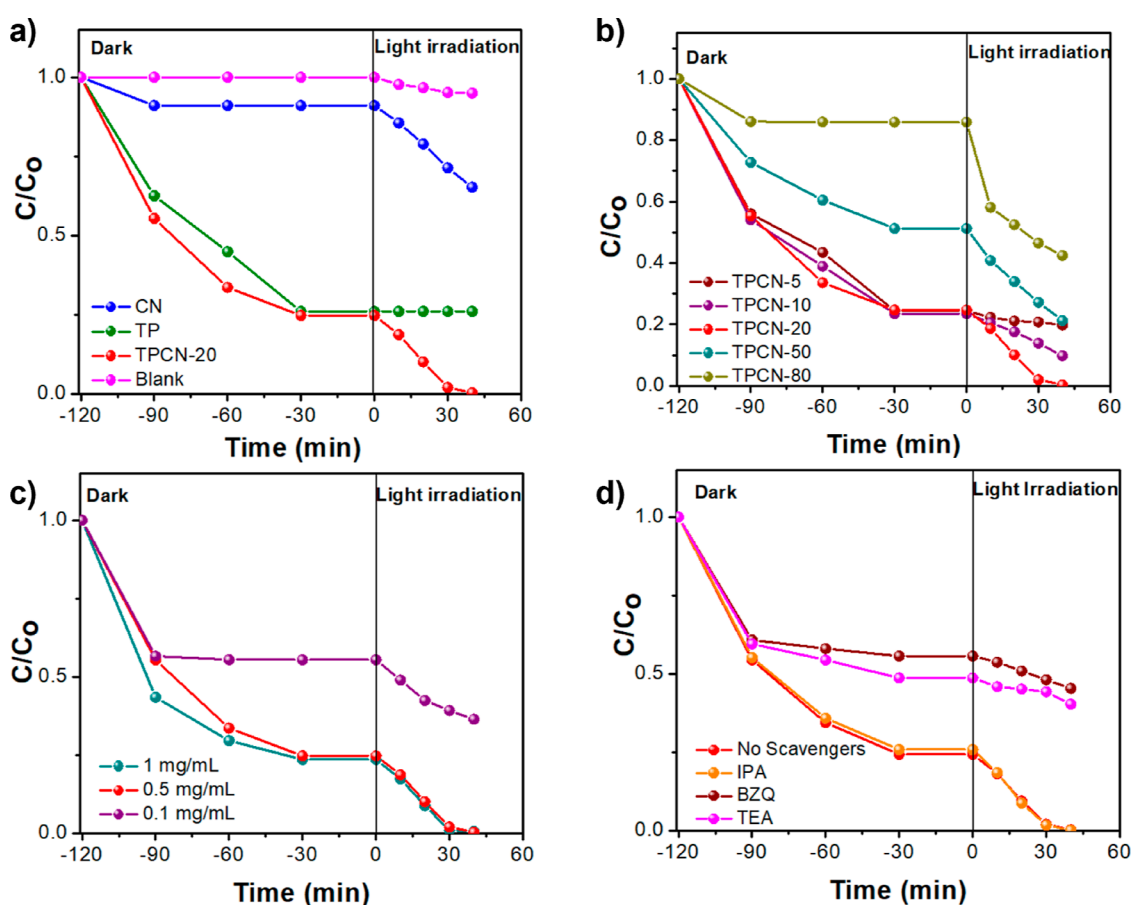

Figure 6. Removal of RhB (20 μM in water). (a) RhB degradation under visible light after equilibration in the dark; blank solution, pure TP (0.5 mg mL^{-1}), pure CN (0.5 mg mL^{-1}), and TPCN-20 (0.5 mg mL^{-1}). (b) RhB degradation under visible light after equilibration in the dark using various catalyst samples (0.5 mg mL^{-1}). (c) Effect of catalyst (TPCN-20) dose on RhB degradation under visible light after equilibration in the dark. (d) Effect of different scavengers on RhB degradation over the TPCN-20 catalyst (0.5 mg mL^{-1}) after equilibration in the dark.

where K_f (mg/g(L/mg)1/n) is the Freundlich constant related to the adsorption capacity and the slope $1/n$ indicates intensity of adsorption or surface heterogeneity in a range between 0 and 1. The values of K_f and n were obtained from the linear plot between ln q_e versus ln C_e, where q_e (mg g^{-1}) is the adsorbed amount of adsorbate at equilibrium and C_e (mg L^{-1}) is the equilibrium concentration of adsorbate (Figure 7 and Table S5).

The analysis shows that RhB adsorption for CN, TP, and TPCN-20 was well described by the Freundlich model, with R^2 values of 0.989, 0.998, and 0.999, respectively. Nevertheless, the R^2 for Langmuir model fitting for CN was also higher than 0.96 (Figure S4), indicating the presence of a partially heterogeneous structure, i.e., multilayer adsorption. These observations confirmed that adsorption on CN, TP, and TPCN-20 was likely to involve a multilayered process with complex adsorption mechanisms, reflecting the heterogeneity
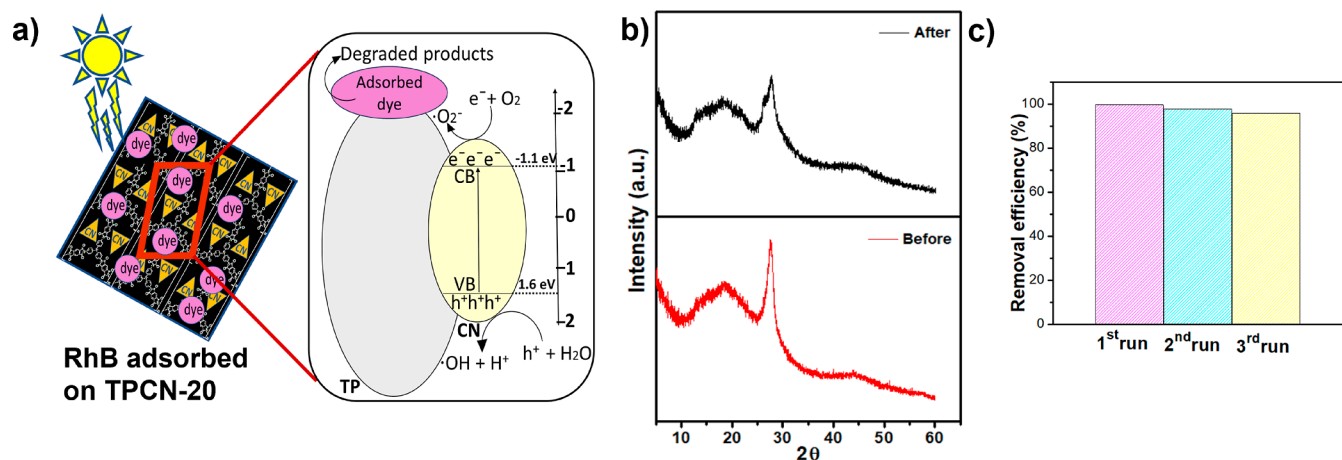
Figure 7. (a) Proposed mechanism for photocatalytic degradation of adsorbed dye over the surface of TPCN under visible light. (b) XRD patterns of TPCN-20 before and after three experimental runs. (c) Removal efficiency of recycled TPCN-20 (0.5 mg mL^{-1}) for three photocatalytic degradation cycles of RhB (20 μM in water).

of the catalyst surface. From the fitting results with the Freundlich model, the n values were evidently >1 for CN, TP, and TPCN-20, indicating that the adsorption might occur through physical interactions, i.e., electrostatic interaction, ion exchange, or synergistic mechanisms on the catalysts surface. The slope value for the catalysts CN, TP, and TPCN-20 is less than 1, indicating that adsorption of RhB dye on TPCN-20 is heterogeneous. Both Langmuir and Freundlich isotherms were found to fit the experimental data, yet the higher regression coefficient R^2 values indicate that the Freundlich isotherm is most appropriate for the adsorption of RhB dye on TPCN-20 (Table S5).

The adsorption mechanism depends on the characteristics of the adsorbent and the mass transport process. To confirm the controlling mechanism of the adsorption process, the pseudo-first order (PFO[46]) and the pseudo-second order (PSO) model were investigated in order to analyze the experimental data of the adsorption of RhB dye onto TPCN-20. Our results show that adsorption kinetics proceed according to a PSO model, which is expressed by the equation

$$\frac{t}{q_t} = \frac{1}{K_2 q_e^2} + \frac{t}{q_e}$$

where K_2 is rate constant for second-order adsorption (g mg^{-1} min^{-1}). K_2 and q_e were determined from slope and intercept of the plot of t/q_t versus t (Figure 5). The calculated q_e values are in good agreement with the experimental q_e values and correlation coefficient (R^2) values are also very close to 1 (Table S5), which together indicate that the adsorption of RhB dye on TPCN-20 follows the second-order kinetic model suggesting that adsorption involves a chemical process that depends on both RhB dye and TPCN-20.

Photocatalytic Properties of TPCN Composites. The photocatalytic activity of the TPCN composites was evaluated via photocatalytic degradation of RhB dye in an aqueous solution under visible light irradiation with a catalyst concentration of 0.5 mg mL^{-1} in RhB solution (20 μM). Figure 6 shows the dye removal curves for all samples under similar conditions of light irradiation, where C_0 and C represent the initial dye concentration and concentration after the reaction time (t), respectively. It can be observed that pure TP reduces RhB concentration significantly. After 120

min of stirring in the dark, an overall RhB removal of 73% is observed due to adsorption. In the case of RhB solution without catalyst loading, no significant change is observed in RhB dye concentration in the time span of 0−40 min of light irradiation, i.e., only a slight decrease of 5% is observed. As noticed before, TP is not a semiconductor and thus does not perform in the catalytic degradation reaction. For pure CN (0.5 mg mL^{-1}), after achieving the adsorption−desorption equilibrium, a slight decrease in RhB dye concentration (34%) under visible light irradiation of 40 min is observed, hence representing the limitation of photocatalytic performance attributed to its ability of fast recombination of electron hole pairs.

However, for the composite samples, i.e., TPCN-X, enhanced RhB dye removal is observed as compared to pristine CN and pure TP, i.e., 99% for TPCN-20 after 40 min. Such an increase in the RhB dye removal for TPCN-X samples might be associated with two key steps: (i) TP in the composite samples acts as an effective dye adsorbent; thus, a moderate amount of RhB dye is adsorbed on the TP and (ii) dye degradation by CN. Hence, among TPCN-X samples, TPCN-80, and TPCN-50 show less adsorption, while the TPCN-10 and TPCN-5 show the highest amount of adsorption. However, TPCN-20 gives the best dye removal results, which indicates the optimum ratio of TP and CN in the catalyst. The improved photocatalytic performance is attributed to the combined impact of enhanced RhB dye adsorption by the TP support and optimum loading of photocatalytic CN particles. Combination of TP with CN improves light harvesting and thus improves catalysis. One of the major drawbacks of traditional photocatalysts is the recombination of the formed electrons (e$^-$) and holes (h$^+$), decreasing catalytic activity. Based on PL analysis, CN had the highest PL intensity, whereas a decreased PL intensity was observed for TPCN-20, suggesting that the composite can suppress the recombination of photogenerated charge carriers. Thus, it is indicated that TP improves the separation efficiency of h$^+$ and e$^-$. Consequently, TPCN composites have photocatalytic properties superior to those of CN and TP.

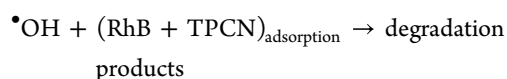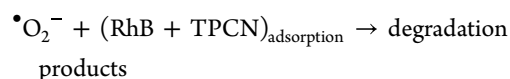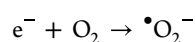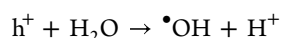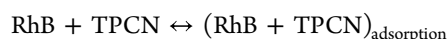The effect of catalyst dose was studied as well and is described in Figure 6c. The dye removal efficiency increased as the catalyst dose increased from 0.1 to 0.5 mg mL^{-1}, which is expected due to the presence of a higher number of active sites.

However, a further increase in the catalyst dose to 1 mg mL^{-1}, led to no obvious change in the dye removal. A constant dye removal efficiency with increasing catalyst dose suggests particle agglomeration as no additional active sites seem to be available. In conclusion, TPCN-20 show an improved efficiency with the synergistic effect of adsorption and photodegradation for RhB removal as compared to the literature (Table S6).[47−52]

Role of Active Species. Several control experiments were performed to investigate the photocatalytic mechanism and the involved active species by adding scavengers into the aqueous RhB solution. For example, superoxide radicals were removed with p-benzoquinone (BZQ, 10 mmol L^{-1}), hydroxyl radicals were removed with isopropanol (IPA, 10 vol %), and holes were removed with triethanolamine (TEA, 10 vol %).[53]

Figure 6d summarizes the photocatalytic efficiencies of RhB with TPCN-20 after the addition of various scavengers. The degradation efficiency remained almost unchanged in the presence of IPA, indicating that the degradation process does not rely on hydroxyl radicals. The addition of TEA and BZQ led to a remarkable decrease in the degradation of RhB. Although both TEA and BZQ led to a decreased adsorption of RhB, the degradation RhB via photocatalysis is impacted significantly by TEA and BZQ after achieving the adsorption equilibrium. From literature, it can be deduced that superoxide radicals are the main active species responsible for photo-catalytic dye degradation driven by pure CN.[54] In the present work, the results indicate that holes are the other major active species generated in the TPCN-20 catalyst system. In view of the above results, it can be proposed that both superoxide radicals and holes are the main active species and play an important role in the working of TPCN for RhB degradation.

Based on the above analysis, a possible photocatalytic degradation mechanism for RhB by TPCN is proposed (Figure 7a). Initially, RhB is adsorbed onto the surface of TPCN. TP in TPCN plays the major role in adsorption, and later, when exposed to visible light, the CN component of TPCN-20 is easily excited due to its narrow band gap to generate photogenerated e$^-$ and h$^+$ pairs. The photogenerated electrons react with dissolved O$_2$ to form the active species of $^\bullet$O^{2-} which is mainly responsible for degradation. Similarly, the photogenerated holes produced are also active in dye oxidation. Here in TPCN, the recombination of photo-generated charge pairs is effectively inhibited, and the charge separation efficiency is enhanced, which is in accordance with PL spectra of the samples.

$$RhB + TPCN \leftrightarrow (RhB + TPCN)_{adsorption}$$

$$TPCN + h\nu \rightarrow TPCN + e^- + h^+$$

$$h^+ + H_2O \rightarrow {}^\bullet OH + H^+$$

$$e^- + O_2 \rightarrow {}^\bullet O_2^-$$

$${}^\bullet O_2^- + (RhB + TPCN)_{adsorption} \rightarrow degradation\ products$$

$${}^\bullet OH + (RhB + TPCN)_{adsorption} \rightarrow degradation\ products$$

Reusability of TPCN Composite. To investigate the stability and reusability of TPCN composites, a catalyst recycling test for photodegradation was performed with TPCN-20. After each photodegradation cycle, the catalyst was collected, rinsed three times with deionized water, and then dried at 80 °C in an oven for further use. The XRD patterns of the TPCN-20 before and after the degradation tests show a high similarity, confirming the catalyst's integrity after the catalytic runs (Figure 7b). Similarly, FT-IR analysis after the photodegradation did not indicate any significant changes, indicating an acceptable stability of the catalyst composite (Figure S5). As depicted in Figure 7c, TPCN-20 showed no obvious reduction of photocatalytic activity after three cycles for RhB degradation, demonstrating its excellent stability and reusability for multiple organic pollutant removal runs for at least three cycles.

■ EXPERIMENTAL SECTION

Materials. Cyanuric acid (98%), dimethyl sulfoxide (DMSO, 99%), ethanol (99.5%), 1-fluoro-4-nitrobenzene (≥99%), hydrazine hydrate (80% in water), melamine (99%), 4-nitroaniline (99%), palladium/charcoal activated (10% Pd), potassium carbonate (≥98%), pyromellitic dianhydride (PMDA, 97%), and rhodamine B (RhB) (>95%) were obtained from Sigma-Aldrich and used as received. Ethanol was purified and dried following standard procedures.

Synthesis of Tris(4-nitrophenyl)amine TNPA. TNPA was synthesized according to a modified literature procedure.[55] 4-Nitroaniline (3 g, 21.7 mmol, 1.0 equiv) was stirred with K$_2$CO$_3$ (6.9 g, 49.9 mmol, 2.3 equiv) in DMSO (10 mL) at ambient temperature for 6 h in a three-neck round-bottom flask outfitted with a magnetic stirrer, condenser, and quick fit thermometer; then, 1-fluoro-4-nitrobenzene (4.7 mL, 47.6 mmol, 2.2 equiv) was added dropwise and refluxed at 120 °C for 48 h. After the completion of the reaction, the reaction mixture was poured onto the crushed ice. A dilute HCl (1 M) solution was used to neutralize the reaction, and yellow to orange precipitate appeared. The solid was filtered and washed with warm ethanol, tris(4-nitrophenyl)amine (TNPA) was obtained in a yield of 6.4 g (16.8 mmol, 77%) with mp >300 °C.

Synthesis of Tris(4-aminophenyl)amine. According to a modified literature procedure,[55] tris(4-nitrophenyl)amine (2.0 g, 5.3 mmol, 1.0 equiv) was dissolved in dry distilled ethanol (100 mL) with palladium on activated charcoal (0.02 g), after 1 h hydrazine hydrate solution (7 mL, 175.0 mmol, 33.0 equiv) was added slowly and the mixture refluxed for 48 h. After the reaction was completed, the palladium charcoal was removed by hot filtration and the surplus ethanol was removed under reduced pressure. As a result, light gray crystals of tris(4-aminophenyl)amine (TAPA) were obtained, filtered, rinsed with distilled water, and dried to receive a yield of 1.57 g (5.4 mmol, quantitative), mp 233−235 °C.

Synthesis of Tris(4-aminophenyl)amine-based Polyimide (TP). Tris(4-aminophenyl)amine-based polyimide (TP) was synthesized by a modified literature procedure.[56] TAPA (290 mg, 1.0 mmol, 1.0 equiv) and pyromellitic dianhydride (PMDA) (327 mg, 1.5 mmol, 1.5 equiv) were mixed uniformly in an agate mortar. Then, the uniform mixture was put into a porcelain crucible with a loosely covered lid and heated to 300 °C with a heating rate of 10 °C min^{-1} in a furnace for 4 h. The resultant solid was ground into a powder in a yield of 580 mg (94%).

Synthesis of Cyanuric Acid-Melamine Derived Graphitic Carbon Nitride. CN was synthesized by a modified literature procedure.[57] Melamine (5.0 g, 39.7 mmol, 1.0 equiv) and cyanuric acid (5.0 g, 38.8 mmol, 1.0 equiv) were mixed in 200 mL of deionized water, and then, the mixture was shaken overnight. Afterward, the precipitate was filtered and freeze-dried. The white solid was introduced into a tube furnace and heated under nitrogen to 550 °C for 4 h, with a heating rate of 2.3 °C min^{-1}. After cooling to ambient temperature, CN (1.9 g, 19%) was collected as a yellow powder.

Synthesis of TPCN Composites. TP was mixed with CN at different weight fractions [TP/CN = 95/5, 90/10, 80/20, 50/50, and

20/80] in absolute ethanol. The mixtures were ultrasonicated for 2 h and then the solvent evaporated at 50 °C. The resultant powders were named as TPCN-5, TPCN-10, TPCN-20, TPCN-50, and TPCN-80, respectively.

Photocatalytic RhB Degradation. In a typical RhB degradation experiment, TPCN composite sample (10 mg) and RhB solution (20 mL, 20 μM) were mixed in a glass vial in the dark under continuous stirring for 120 min to achieve an adsorption−desorption equilibrium. After that, the mixtures were placed between two white 50 W LEDS (Bridge lux BXRA-50C5300; $\lambda > 410$ nm) and irradiated. The adsorption and photodegradation of RhB was monitored by a decrease in dye concentration. Several samples were collected at certain time intervals. The RhB concentration was measured spectrophotometrically utilizing its absorption maximum ($\lambda = 554$ nm) and plotted as normalized concentration C/C_0. As a reference, the same experiment was performed with TP and CN only. A blank experiment in the absence of the photocatalysts under light irradiation was performed, as well.

To investigate the photocatalytic mechanism, degradation experiments were performed with 10 vol % triethanolamine, 10 vol % isopropanol, and a solution containing 10 mM benzoquinone solution. Other experimental processes were similar to those of the photocatalytic degradation of RhB.

The removal efficiency of RhB (DR) was calculated by using the following equation

$$DR = \left(\frac{C_o - C_e}{C_o} \right) \times 100$$

where C_o (mg L^{-1}) denotes the initial concentration and C_e (mg L^{-1}) denotes the concentration in equilibrium.

Adsorption Evaluation. 10 mg portion of each respective sample was dispersed into 20 mL of RhB dye solution and stirred in the dark. During the adsorption period, samples were taken after every 10 min and analyzed using UV−vis absorption spectra.

The adsorption capacity (mg g^{-1}) and efficiency (%) of selected samples at equilibrium (q_e) and at time t (q_t) were calculated by using the following equations

$$q_t = \frac{(C_o - C_t)V}{W}$$

$$\text{adsorption efficiency (\%)} = \left(\frac{C_o - C_e}{C_o} \right) \times 100$$

where C_o (mg L^{-1}) is the initial concentration and C (mg L^{-1}) is the concentration at time t, V is the volume of solution (L), and W is the mass of photocatalyst (g).

Analytical Methods. FTIR spectra were recorded using a Jasco FTIR-4100. XRD patterns of TP, CN, and their composites were obtained using a Miniflex by Rigaku. SEM was performed on a FEI XL30 ESEM to detect the morphology of TP, CN, and TPCN-20. Nitrogen adsorption−desorption isotherm measurements were carried out on QUADRASORB evo by Anton Parr, and BET surface area calculations were done using QuadraWin Software. The nitrogen adsorption and desorption isotherms were measured after the samples were degassed on a FloVac instrument. PL of TP, CN, and TPCN-20 was measured via Duetta-Bio by Horiba. Solid-state UV−vis spectroscopy of TP, CN, and TPCN-20 were recorded via diffuse reflectance accessory on a Cary 100 spectrophotometer to calculate the band gap energies. UV−vis for photocatalysis investigation was performed with a Shimadzu UV-3600 UV−vis−NIR spectrometer. Ultrasonication was performed via an ultrasonicator at 50% amplitude (Fisherbrand 120 Sonic Dismembrator). Solid-state ^{13}C NMR was recorded on a 300 MHz Bruker WB UltraShield 2 channel instrument with a 4 mm WB MAS ^{15}N−^{31}P/^{1}H broadband probe.

Calculations. All DFT calculations were performed using the Gaussian 09 suite of programmes.[58] We employed the B3LYP hybrid functional[59] with a Coulomb-attenuating correction (CAM-B3LYP),[60] in combination with a cc-pVDZ basis set.[61] The effect of solvation by a polar solvent (acetonitrile) was modeled using a polarizable continuum model (scf = pcm).[62,63] DLPNO−CCSD(T) single point energy calculations[64−66] were performed in combination with Ahlrich's def2-TZVP basis set[67,68] using ORCA version 4.2.1.[69,70] Solvation by acetonitrile was taken on account of using the CPCM method.[71]

CONCLUSIONS

This work reports preparation of polyimide composites with synergistic adsorption and photocatalytic degradation performance for the removal of organic dyes by combination with a well-known photocatalyst, graphitic carbon nitride. The composite catalyst showed considerable adsorption of organic dyes in the dark. Graphitic carbon nitride particles were uniformly distributed on the surface of the polyimide to impart the composite with photodegradation activity for the dyes. A synergistic effect between adsorption and photocatalytic activity between both components was observed. Furthermore, the catalyst could be reused several times with only a minor loss in activity. This work provides insights into the design of high-performance materials with adsorption and photocatalytic properties for wastewater remediation.

ASSOCIATED CONTENT

Ⓢ Supporting Information

The Supporting Information is available free of charge at https://pubs.acs.org/doi/10.1021/acsapm.4c00019.

> Additional information on crystallinity, adsorption data, details about computational data, and comparison with literature performance (PDF)

AUTHOR INFORMATION

Corresponding Authors

Humaira Masood Siddiqi − *Department of Chemistry, Quaid-i-Azam University, Islamabad 45320, Pakistan;* ⓞ orcid.org/0000-0002-9634-9383; Email: humairas@qau.edu.pk

Bernhard V. K. J. Schmidt − *School of Chemistry, University of Glasgow, Glasgow G12 8QQ, U.K.;* ⓞ orcid.org/0000-0002-3580-7053; Email: bernhard.schmidt@glasgow.ac.uk

Authors

Umama Binte Irshad − *School of Chemistry, University of Glasgow, Glasgow G12 8QQ, U.K.; Department of Chemistry, Quaid-i-Azam University, Islamabad 45320, Pakistan*

Zareen Akhtar − *Department of Chemistry, Quaid-i-Azam University, Islamabad 45320, Pakistan*

Götz Bucher − *School of Chemistry, University of Glasgow, Glasgow G12 8QQ, U.K.*

Alexey Y. Ganin − *School of Chemistry, University of Glasgow, Glasgow G12 8QQ, U.K.;* ⓞ orcid.org/0000-0002-3754-5819

Complete contact information is available at:
https://pubs.acs.org/10.1021/acsapm.4c00019

Notes

The authors declare no competing financial interest.

ACKNOWLEDGMENTS

■ REFERENCES

(1) Preisner, M.; Neverova-Dziopak, E.; Kowalewski, Z. An Analytical Review of Different Approaches to Wastewater Discharge Standards with Particular Emphasis on Nutrients. *Environ. Manage.* **2020**, *66* (4), 694−708.

(2) Albalwi, H. A. Synthesis and Characterization of Ca-ALG/MgO/ Ag Nanocomposite Beads for Catalytic Degradation of Direct Red Dye. *Catalysts* **2023**, *13* (1), 78.

(3) Cheng, S.; Zhao, S.; Xing, B.; Liu, Y.; Zhang, C.; Xia, H. Preparation of Magnetic Adsorbent-Photocatalyst Composites for Dye Removal by Synergistic Effect of Adsorption and Photocatalysis. *J. Cleaner Prod.* **2022**, *348*, 131301.

(4) Cheng, L.; Zhang, Y.; Fan, W.; Ji, Y. Synergistic Adsorption-Photocatalysis for Dyes Removal by a Novel Biochar-Based Z-Scheme Heterojunction BC/2ZIS/WO₃: Mechanistic Investigation and Degradation Pathways. *Chem. Eng. J.* **2022**, *445*, 136677.

(5) Rauf, M. A.; Meetani, M. A.; Khaleel, A.; Ahmed, A. Photocatalytic Degradation of Methylene Blue Using a Mixed Catalyst and Product Analysis by LC/MS. *Chem. Eng. J.* **2010**, *157* (2−3), 373−378.

(6) Li, T.; Zhao, L.; He, Y.; Cai, J.; Luo, M.; Lin, J. Synthesis of g-C₃N₄/SmVO₄ Composite Photocatalyst with Improved Visible Light Photocatalytic Activities in RhB Degradation. *Appl. Catal., B* **2013**, *129*, 255−263.

(7) Alotaibi, K. M.; Almethen, A. A.; Beagan, A. M.; Al-Swaidan, H. M.; Ahmad, A.; Bhawani, S. A.; Alswieleh, A. M. Quaternization of Poly(2-Diethyl Aminoethyl Methacrylate) Brush-Grafted Magnetic Mesoporous Nanoparticles Using 2-Iodoethanol for Removing Anionic Dyes. *Appl. Sci.* **2021**, *11* (21), 10451.

(8) Kariyajjanavar, P.; Jogttappa, N.; Nayaka, Y. A. Studies on Degradation of Reactive Textile Dyes Solution by Electrochemical Method. *J. Hazard. Mater.* **2011**, *190* (1−3), 952−961.

(9) Nandhini, N. T.; Rajeshkumar, S.; Mythili, S. The Possible Mechanism of Eco-Friendly Synthesized Nanoparticles on Hazardous Dyes Degradation. *Biocatal. Agric. Biotechnol.* **2019**, *19*, 101138.

(10) Zhu, G.; Fang, H.; Xiao, Y.; Hursthouse, A. S. The Application of Fluorescence Spectroscopy for the Investigation of Dye Degradation by Chemical Oxidation. *J. Fluoresc.* **2020**, *30* (5), 1271−1279.

(11) Lucaci, A. R.; Bulgariu, D.; Ahmad, I.; Bulgariu, L. Equilibrium and Kinetics Studies of Metal Ions Biosorption on Alginate Extracted from Marine Red Algae Biomass (Callithamnion Corymbosum Sp.). *Polymers* **2020**, *12* (9), 1888.

(12) Stejskal, J. Interaction of Conducting Polymers, Polyaniline and Polypyrrole, with Organic Dyes: Polymer Morphology Control, Dye Adsorption and Photocatalytic Decomposition. *Chem. Pap.* **2020**, *74* (1), 1−54.

(13) Ahmadi, Y.; Kim, K.-H. Hyperbranched Polymers as Superior Adsorbent for the Treatment of Dyes in Water. *Adv. Colloid Interface Sci.* **2022**, *302*, 102633.

(14) Zhao, X.; Jiang, X.; Peng, D.; Teng, J.; Yu, J. Behavior and Mechanism of Graphene Oxide-Tris(4-Aminophenyl)Amine Composites in Adsorption of Rare Earth Elements. *J. Rare Earths* **2021**, *39* (1), 90−97.

(15) Yan, K.; Chen, H.; Zhu, C.; Ke, Z.; Li, D.; Wang, M.; Dai, F.; Yu, Y. Synthesis and Characterization of Novel Triphenylamine—Containing Electrochromic Polyimides with Benzimidazole Substituents. *Molecules* **2023**, *28* (5), 2029.

(16) Jiang, L.; Messing, M. E.; Ye, L. Temperature and PH Dual-Responsive Core-Brush Nanocomposite for Enrichment of Glycoproteins. *ACS Appl. Mater. Interfaces* **2017**, *9* (10), 8985−8995.

(17) Pradhan, G. K.; Parida, K. Fabrication of Iron-Cerium Mixed Oxide: An Efficient Photocatalyst for Dye Degradation. *Int. J. Eng. Sci. Technol.* **2011**, *2* (8), 53.

(18) Chen, X.; Wu, Z.; Liu, D.; Gao, Z. Preparation of ZnO Photocatalyst for the Efficient and Rapid Photocatalytic Degradation of Azo Dyes. *Nanoscale Res. Lett.* **2017**, *12* (1), 143.

(19) Saravanan, R.; Sacari, E.; Gracia, F.; Khan, M. M.; Mosquera, E.; Gupta, V. K. Conducting PANI Stimulated ZnO System for Visible Light Photocatalytic Degradation of Coloured Dyes. *J. Mol. Liq.* **2016**, *221*, 1029−1033.

(20) Kumar, S. G.; Rao, K. K. Comparison of Modification Strategies towards Enhanced Charge Carrier Separation and Photocatalytic Degradation Activity of Metal Oxide Semiconductors (TiO₂, WO₃ and ZnO). *Appl. Surf. Sci.* **2017**, *391*, 124−148.

(21) Mahmoodi, N. M.; Arami, M.; Limaee, N. Y.; Tabrizi, N. S. Kinetics of Heterogeneous Photocatalytic Degradation of Reactive Dyes in an Immobilized TiO₂ Photocatalytic Reactor. *J. Colloid Interface Sci.* **2006**, *295* (1), 159−164.

(22) Elango, G.; Roopan, S. M. Efficacy of SnO₂ Nanoparticles toward Photocatalytic Degradation of Methylene Blue Dye. *J. Photochem. Photobiol., B* **2016**, *155*, 34−38.

(23) Abdelrahman, E. A.; Hegazey, R. M.; Kotp, Y. H.; Alharbi, A. Facile Synthesis of Fe₂O₃ Nanoparticles from Egyptian Insecticide Cans for Efficient Photocatalytic Degradation of Methylene Blue and Crystal Violet Dyes. *Spectrochim. Acta, Part A* **2019**, *222*, 117195.

(24) Dong, S.; Cui, Y.; Wang, Y.; Li, Y.; Hu, L.; Sun, J.; Sun, J. Designing Three-Dimensional Acicular Sheaf Shaped BiVO₄/ Reduced Graphene Oxide Composites for Efficient Sunlight-Driven Photocatalytic Degradation of Dye Wastewater. *Chem. Eng. J.* **2014**, *249*, 102−110.

(25) Li, R.; Song, X.; Huang, Y.; Fang, Y.; Jia, M.; Ma, W. Visible-Light Photocatalytic Degradation of Azo Dyes in Water by Ag₃PO₄: An Unusual Dependency between Adsorption and the Degradation Rate on PH Value. *J. Mol. Catal. A: Chem.* **2016**, *421*, 57−65.

(26) Cao, S.; Low, J.; Yu, J.; Jaroniec, M. Polymeric Photocatalysts Based on Graphitic Carbon Nitride. *Adv. Mater.* **2015**, *27* (13), 2150−2176.

(27) Thomas, A.; Fischer, A.; Goettmann, F.; Antonietti, M.; Müller, J. O.; Schlögl, R.; Carlsson, J. M. Graphitic Carbon Nitride Materials: Variation of Structure and Morphology and Their Use as Metal-Free Catalysts. *J. Mater. Chem.* **2008**, *18* (41), 4893.

(28) Jun, Y.; Hong, W. H.; Antonietti, M.; Thomas, A. Mesoporous, 2D Hexagonal Carbon Nitride and Titanium Nitride/Carbon Composites. *Adv. Mater.* **2009**, *21* (42), 4270−4274.

(29) Patnaik, S.; Martha, S.; Acharya, S.; Parida, K. M. An Overview of the Modification of g-C₃ N₄ with High Carbon Containing Materials for Photocatalytic Applications. *Inorg. Chem. Front.* **2016**, *3* (3), 336−347.

(30) Wang, X.; Maeda, K.; Thomas, A.; Takanabe, K.; Xin, G.; Carlsson, J. M.; Domen, K.; Antonietti, M. A Metal-Free Polymeric Photocatalyst for Hydrogen Production from Water under Visible Light. *Nat. Mater.* **2009**, *8* (1), 76−80.

(31) Kumru, B.; Barrio, J.; Zhang, J.; Antonietti, M.; Shalom, M.; Schmidt, B. V. K. J. Robust Carbon Nitride-Based Thermoset Coatings for Surface Modification and Photochemistry. *ACS Appl. Mater. Interfaces* **2019**, *11* (9), 9462−9469.

(32) Cao, Q.; Barrio, J.; Antonietti, M.; Kumru, B.; Shalom, M.; Schmidt, B. V. K. J. Photoactive Graphitic Carbon Nitride-Based Gel Beads As Recyclable Photocatalysts. *ACS Appl. Polym. Mater.* **2020**, *2* (8), 3346−3354.

(33) Chen, G.; Zhou, Z.; Li, B.; Lin, X.; Yang, C.; Fang, Y.; Lin, W.; Hou, Y.; Zhang, G.; Wang, S. S-Scheme Heterojunction of Crystalline Carbon Nitride Nanosheets and Ultrafine WO3 Nanoparticles for Photocatalytic CO₂ Reduction. *J. Environ. Sci.* **2024**, *140*, 103−112.

(34) Wang, R.; Yang, P.; Wang, S.; Wang, X. Distorted Carbon Nitride Nanosheets with Activated n → Π* Transition and Preferred Textural Properties for Photocatalytic CO₂ Reduction. *J. Catal.* **2021**, *402*, 166−176.

(35) Zhang, J.; Ye, G.; Zhang, C.; Pan, Z.; Wang, S.; Zhang, G.; Wang, X. Heptazine-Based Ordered-Distorted Copolymers with Enhanced Visible-Light Absorption for Photocatalytic Hydrogen Production. *ChemSusChem* **2022**, *15* (24), No. e202201616.

(36) Zhao, Z.; Sun, Y.; Dong, F. Graphitic Carbon Nitride Based Nanocomposites: A Review. *Nanoscale* **2015**, *7* (1), 15−37.

(37) Hsiao, S.-H.; Chen, W.-T. Syntheses and Properties of Aromatic Polyimides Based on 1, 1-Bis [4-(4-Aminophenoxy)

Phenyl]-1-Phenyl-2, 2, 2-Trifluoroethane and 1, 1-Bis [4-(4-Amino-phenoxy) Phenyl]-1-Phenylethane. *J. Polym. Res.* **2003**, *10*, 95−103.

(38) Cao, J.; Qin, C.; Wang, Y.; Zhang, H.; Sun, G.; Zhang, Z. Solid-State Method Synthesis of SnO$_2$-Decorated g-C$_3$N$_4$ Nanocomposites with Enhanced Gas-Sensing Property to Ethanol. *Materials* **2017**, *10* (6), 604.

(39) Fang, J.; Kita, H.; Okamoto, K. Hyperbranched Polyimides for Gas Separation Applications. 1. Synthesis and Characterization. *Macromolecules* **2000**, *33* (13), 4639−4646.

(40) Paul, D. R.; Sharma, R.; Nehra, S. P.; Sharma, A. Effect of Calcination Temperature, PH and Catalyst Loading on Photo-degradation Efficiency of Urea Derived Graphitic Carbon Nitride towards Methylene Blue Dye Solution. *RSC Adv.* **2019**, *9* (27), 15381−15391.

(41) Belhamdi, B.; Merzougui, Z.; Trari, M.; Addoun, A. A Kinetic, Equilibrium and Thermodynamic Study of l-Phenylalanine Adsorp-tion Using Activated Carbon Based on Agricultural Waste (Date Stones). *J. Appl. Res. Technol.* **2016**, *14* (5), 354−366.

(42) Pawar, R. C.; Khare, V.; Lee, C. S. Hybrid Photocatalysts Using Graphitic Carbon Nitride/Cadmium Sulfide/Reduced Graphene Oxide (g-C$_3$ N$_4$/CdS/RGO) for Superior Photodegradation of Organic Pollutants under UV and Visible Light. *Dalton Trans.* **2014**, *43* (33), 12514−12527.

(43) Oishi, Y.; Ishida, M.; Kakimoto, M.; Imai, Y.; Kurosaki, T. Preparation and Properties of Novel Soluble Aromatic Polyimides from 4,4′-diaminotriphenylamine and Aromatic Tetracarboxylic Dianhydrides. *J. Polym. Sci., Part A: Polym. Chem.* **1992**, *30* (6), 1027−1035.

(44) Fazal, T.; Razzaq, A.; Javed, F.; Hafeez, A.; Rashid, N.; Amjad, U. S.; Ur Rehman, M. S.; Faisal, A.; Rehman, F. Integrating Adsorption and Photocatalysis: A Cost Effective Strategy for Textile Wastewater Treatment Using Hybrid Biochar-TiO$_2$ Composite. *J. Hazard. Mater.* **2020**, *390*, 121623.

(45) Benderdouche, N.; Bestani, B.; Hamzaoui, M. The Use of Linear and Nonlinear Methods for Adsorption Isotherm Optimization of Basic Green 4-Dye onto Sawdust-Based Activated Carbon. *J. Mater. Environ. Sci.* **2018**, *9* (4), 1110−1118.

(46) Rajoriya, S.; Saharan, V. K.; Pundir, A. S.; Nigam, M.; Roy, K. Adsorption of Methyl Red Dye from Aqueous Solution onto Eggshell Waste Material: Kinetics, Isotherms and Thermodynamic Studies. *Curr. Res. Green Sustainable Chem.* **2021**, *4*, 100180.

(47) Bhavsar, K. S.; Labhane, P. K.; Dhake, R. B.; Sonawane, G. H. Solvothermal Synthesis of Activated Carbon Loaded CdS Nano-flowers: Boosted Photodegradation of Dye by Adsorption and Photocatalysis Synergy. *Chem. Phys. Lett.* **2020**, *744*, 137202.

(48) Li, X.; Qi, F.; Xue, Y.; Yu, C.; Jia, H.; Bai, Y.; Wang, S.; Liu, Z.; Zhang, J.; Tang, C. Porous Boron Nitride Coupled with CdS for Adsorption-Photocatalytic Synergistic Removal of RhB. *RSC Adv.* **2016**, *6* (101), 99165−99171.

(49) Xu, Y.; Lin, W.; Wang, H.; Guo, J.; Yuan, D.; Bao, J.; Sun, S.; Zhao, W.; Zhao, C. Dual-Functional Polyethersulfone Composite Nanofibrous Membranes with Synergistic Adsorption and Photo-catalytic Degradation for Organic Dyes. *Compos. Sci. Technol.* **2020**, *199*, 108353.

(50) Shi, J.; Chen, T.; Guo, C.; Liu, Z.; Feng, S.; Li, Y.; Hu, J. The Bifunctional Composites of AC Restrain the Stack of G-C$_3$N$_4$ with the Excellent Adsorption-Photocatalytic Performance for the Removal of RhB. *Colloids Surf., A* **2019**, *580*, 123701.

(51) Li, S.; Shen, X.; Liu, J.; Zhang, L. Synthesis of Ta$_3$N$_5$/Bi$_2$MoO$_6$ Core-Shell Fiber-Shaped Heterojunctions as Efficient and Easily Recyclable Photocatalysts. *Environ. Sci.: Nano* **2017**, *4* (5), 1155−1167.

(52) Wu, X.; Liu, C.; Li, X.; Zhang, X.; Wang, C.; Liu, Y. Effect of Morphology on the Photocatalytic Activity of g-C$_3$N$_4$ Photocatalysts under Visible-Light Irradiation. *Mater. Sci. Semicond. Process.* **2015**, *32*, 76−81.

(53) Wang, L.; Li, Y.; Han, P. Electrospinning Preparation of G-C3N4/Nb2O5 Nanofibers Heterojunction for Enhanced Photo-

catalytic Degradation of Organic Pollutants in Water. *Sci. Rep.* **2021**, *11* (1), 22950.

(54) Tian, Y.; Chang, B.; Lu, J.; Fu, J.; Xi, F.; Dong, X. Hydrothermal Synthesis of Graphitic Carbon Nitride-Bi$_2$ WO$_6$ Heterojunctions with Enhanced Visible Light Photocatalytic Activities. *ACS Appl. Mater. Interfaces* **2013**, *5* (15), 7079−7085.

(55) EL-Mahdy, A. F. M.; Kuo, C.-H.; Alshehri, A.; Young, C.; Yamauchi, Y.; Kim, J.; Kuo, S.-W. Strategic Design of Triphenyl-amine- and Triphenyltriazine-Based Two-Dimensional Covalent Organic Frameworks for CO$_2$ Uptake and Energy Storage. *J. Mater. Chem. A* **2018**, *6* (40), 19532−19541.

(56) Maschita, J.; Banerjee, T.; Savasci, G.; Haase, F.; Ochsenfeld, C.; Lotsch, B. V. Ionothermal Synthesis of Imide-Linked Covalent Organic Frameworks. *Angew. Chem.* **2020**, *132* (36), 15880−15888.

(57) Shalom, M.; Inal, S.; Fettkenhauer, C.; Neher, D.; Antonietti, M. Improving Carbon Nitride Photocatalysis by Supramolecular Preorganization of Monomers. *J. Am. Chem. Soc.* **2013**, *135* (19), 7118−7121.

(58) Maschita, J.; Banerjee, T.; Savasci, G.; Haase, F.; Ochsenfeld, C.; Lotsch, B. V. Ionothermal Synthesis of Imide-Linked Covalent Organic Frameworks. *Angew. Chem., Int. Ed.* **2020**, *59* (36), 15750−15758.

(59) Becke, A. D. Density-Functional Thermochemistry. I. The Effect of the Exchange-Only Gradient Correction. *J. Chem. Phys.* **1992**, *96* (3), 2155−2160.

(60) Lee, C.; Yang, W.; Parr, R. G. Development of the Colle-Salvetti Correlation-Energy Formula into a Functional of the Electron Density. *Phys. Rev. B* **1988**, *37* (2), 785−789.

(61) Yanai, T.; Tew, D. P.; Handy, N. C. A New Hybrid Exchange-Correlation Functional Using the Coulomb-Attenuating Method (CAM-B3LYP). *Chem. Phys. Lett.* **2004**, *393* (1−3), 51−57.

(62) Tomasi, J.; Mennucci, B.; Cammi, R. Quantum Mechanical Continuum Solvation Models. *Chem. Rev.* **2005**, *105* (8), 2999−3094.

(63) Cossi, M.; Barone, V.; Cammi, R.; Tomasi, J. Ab Initio Study of Solvated Molecules: A New Implementation of the Polarizable Continuum Model. *Chem. Phys. Lett.* **1996**, *255* (4−6), 327−335.

(64) Riplinger, C.; Sandhoefer, B.; Hansen, A.; Neese, F. Natural Triple Excitations in Local Coupled Cluster Calculations with Pair Natural Orbitals. *J. Chem. Phys.* **2013**, *139* (13), 134101.

(65) Riplinger, C.; Neese, F. An Efficient and near Linear Scaling Pair Natural Orbital Based Local Coupled Cluster Method. *J. Chem. Phys.* **2013**, *138* (3), 034106.

(66) Riplinger, C.; Pinski, P.; Becker, U.; Valeev, E. F.; Neese, F. Sparse Maps—A Systematic Infrastructure for Reduced-Scaling Electronic Structure Methods. II. Linear Scaling Domain Based Pair Natural Orbital Coupled Cluster Theory. *J. Chem. Phys.* **2016**, *144* (2), 024109.

(67) Weigend, F. Accurate Coulomb-Fitting Basis Sets for H to Rn. *Phys. Chem. Chem. Phys.* **2006**, *8* (9), 1057.

(68) Weigend, F.; Ahlrichs, R. Balanced Basis Sets of Split Valence, Triple Zeta Valence and Quadruple Zeta Valence Quality for H to Rn: Design and Assessment of Accuracy. *Phys. Chem. Chem. Phys.* **2005**, *7* (18), 3297.

(69) Neese, F. The ORCA Program System. *Wiley Interdiscip. Rev.: Comput. Mol. Sci.* **2012**, *2* (1), 73−78.

(70) Neese, F. Software Update: The ORCA Program System, Version 4.0. *Wiley Interdiscip. Rev.: Comput. Mol. Sci.* **2018**, *8* (1), No. e1327.

(71) Barone, V.; Cossi, M. Quantum Calculation of Molecular Energies and Energy Gradients in Solution by a Conductor Solvent Model. *J. Phys. Chem. A* **1998**, *102* (11), 1995−2001.

L